

## Article

# Property Improvement of Additively Manufactured Ti64 by Heat Treatment Characterized by In Situ High Temperature EBSD and Neutron Diffraction

Shigehiro Takajo <sup>1</sup>, Toshiro Tomida <sup>2</sup>, El'ad N. Caspi <sup>3</sup>, Asaf Pesach <sup>3</sup>, Eitan Tiferet <sup>4,5</sup> and Sven C. Vogel <sup>6,\*</sup><sup>1</sup> Steel Research Laboratory, JFE Steel Corporation, Chiba 260-0835, Japan; s-takajo@jfe-steel.co.jp<sup>2</sup> Frontier Research Center for Applied Atomic Sciences, Ibaraki University, Naka 319-1106, Japan; toshiro.tomida.tomida\_tsr@vc.ibaraki.ac.jp<sup>3</sup> Physics Department, Nuclear Research Center Negev, Beer-Sheva 84190, Israel; eladc@iaec.gov.il (E.N.C.); asafps@yahoo.com (A.P.)<sup>4</sup> Materials Engineering Department, Nuclear Research Centre Negev, Beer-Sheva 84190, Israel; eitant@nrcn.gov.il<sup>5</sup> Rotem Industries Ltd., Mishor Yamin 86800, Israel<sup>6</sup> Materials Science and Technology Division, Los Alamos National Laboratory, Los Alamos, NM 87545, USA

\* Correspondence: sven@lanl.gov



**Citation:** Takajo, S.; Tomida, T.; Caspi, E.N.; Pesach, A.; Tiferet, E.; Vogel, S.C. Property Improvement of Additively Manufactured Ti64 by Heat Treatment Characterized by In Situ High Temperature EBSD and Neutron Diffraction. *Metals* **2021**, *11*, 1661. <https://doi.org/10.3390/met11101661>

Academic Editors: Oleg Mishin and Soran Biroscu

Received: 7 September 2021

Accepted: 13 October 2021

Published: 19 October 2021

**Publisher's Note:** MDPI stays neutral with regard to jurisdictional claims in published maps and institutional affiliations.



**Copyright:** © 2021 by the authors. Licensee MDPI, Basel, Switzerland. This article is an open access article distributed under the terms and conditions of the Creative Commons Attribution (CC BY) license (<https://creativecommons.org/licenses/by/4.0/>).

**Abstract:** Among various off-equilibrium microstructures of additively manufactured Ti-6Al-4V alloy, electron beam powder bed fusion, in which three dimensional metallic objects are fabricated by melting the ingredient powder materials layer by layer on a pre-heated bed, results in a specimen that is nearly free of the preferred orientation of the  $\alpha$ -Ti phase as well as a low beta phase fraction of  $\sim 1$  wt%. However, when further heat treatment of up to 1050 °C was applied to the material in our previous study, a strong texture aligning the hexagonal basal plane of  $\alpha$  phase with the build direction and about 6%  $\beta$  phase appeared at room temperature. In this study, to understand the mechanism of this heat treatment, the grain level microstructure of the additively manufactured Ti-6Al-4V was investigated using in situ high temperature EBSD up to 1000 °C, which allows the tracking of individual grains during a heat cycle. As a result, we found a random texture originating from the fine grains in the initial material and observed a significant suppression of  $\alpha$  phase nucleation in the slow cooling after heating to 950 °C within the  $\alpha$  and  $\beta$  dual phase regime but close to the  $\beta$ -transus temperature at  $\sim 980$  °C, which led to a coarse microstructure. Furthermore, the texture resulting from phase transformation of the additively manufactured Ti-6Al-4V assuming nucleation at the grain boundaries was modeled, using the double Burgers orientation relationship for the first time. The model successfully reproduced the measured texture, suggesting that the texture enhancement of the  $\alpha$  phase by the additional heat treatment derives also from the variant selection during the phase transformation and nucleation on grain boundaries.

**Keywords:** Ti-6Al-4V; additive manufacturing; texture; transformation; in situ EBSD

## 1. Introduction

Titanium alloy Ti-6Al-4V (wt.%) offers excellent formability, fatigue and creep strength, originating from the balanced  $\alpha$  and  $\beta$ -Ti crystallographic phases and therefore is widely used in the aerospace industry [1,2]. Recently, with the advent of additive manufacturing (AM) technology [3], a lot of research regarding fabrication and characterizations of this light-weighted titanium alloy was reported [4–7]. Powder bed fusion is one of the major AM processes, in which three-dimensional metallic objects are fabricated by melting the ingredient powder materials layer by layer on a platform of a pre-heated powder bed. Our preliminary bulk characterization, using pulsed neutron diffraction, revealed that an additively manufactured sample processed by electron beam powder bed fusion (EB-PBF) method showed little preferential orientation of the  $\alpha$  phase, whereas that of laser

powder bed fusion method showed significant preference towards the hexagonal basal plane, becoming oriented along the build direction [8]. Furthermore, the weight percentage of the  $\beta$  phase of the sample processed with EB-PBF method was found to be  $\sim 1$  wt.%, significantly lower than conventional hot-rolled samples, resulting in weight fractions of 5–7 wt.% for the  $\beta$  phase [9,10].

Figure 1 shows the phase fractions of  $\alpha$  and  $\beta$  phase in Ti-6Al-4V predicted using the Thermo-Calc [11]. Based on the equilibrium calculation of crystallographic phase fraction as a function of temperature, the phase fraction of the  $\alpha$  phase is nearly 100% at room temperature but becomes zero at temperatures higher than 940 °C. The cooling rate during the AM process is estimated to be fast enough [12] for the microstructure to be off equilibrium, which typically leads to a remaining high temperature  $\beta$  phase different from the experimental data of an as-built material processed with the EB-PBF method [13]. Since the phase balance is critical to the mechanical properties of the Ti-6Al-4V, the mechanism of the  $\beta$  phase suppression needs to be clarified to control the material properties. With this motivation, our previous neutron diffraction study [13] was expanded to an in situ high temperature environment up to 1050 °C using a heating chamber, where the microstructure was characterized as a function of temperature, including the  $\alpha$  to  $\beta$  to  $\alpha$  transformation. A peculiar finding was that starting from a preferred orientation of hexagonal basal planes aligned with the build direction with a maximum pole density of  $\sim 2.5$  mrd, after the cycling through the phase transformation, the maximum pole density of the (002) poles aligned parallel to the build direction doubled to  $\sim 5$  mrd. Furthermore, the  $\beta$  phase fraction retained at room temperature increased from  $\sim 1$  wt.% to  $\sim 6$  wt.% before and after the heat treatment, respectively. The measured texture failed to be reproduced by a conventional texture modeling without considering variant selection [13]. There are many additional studies [14–19] on the influence of heat treatment on microstructure and mechanical properties of the Ti-6Al-4V. Katzarov [20] successfully modeled that a high cooling rate results in a large amount of  $\alpha$  phase and a suppressed rate of nucleation of the  $\alpha$  phase depending on the diffusion of vanadium in the material.

The texture enhancement was also reported in conventional Ti-6Al-4V samples [10,21]. Several papers have discussed possible variant selection in  $\beta$  to  $\alpha$  transformation [22–25]. Lonardelli et al. suggested that a preferable grain growth of existing  $\alpha$  phase grains is also responsible for variant selection. Obasi et al. suggested that only the  $\alpha$  variant nucleated in the early stage can survive when the  $\beta$  phase grain is large, leading to a strong  $\alpha$  texture [10,21]. Although these various studies indicate that the texture evolution relates to phase transformation, the difficulty in direct observation of the transformation hinders deep understanding of the mechanism [26]. In this manuscript, two new experimental and modeling approaches are applied to further understand the microstructure evolution of the Ti-6Al-4V processed by the EB-PBF method: the grain level analysis using in situ heating EBSD method, and the phase transformation texture modeling taking into account two neighboring grain pairs simultaneously, which satisfy the Burgers orientation relationship (BOR).

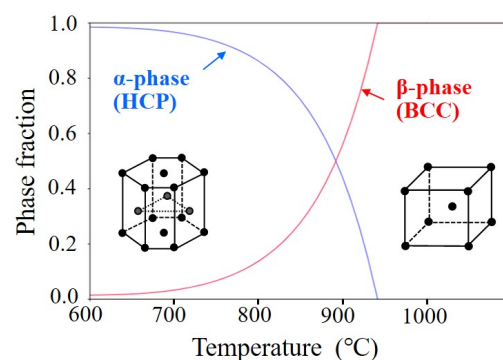


**Figure 1.** Phase fraction of Ti-6Al-4V.

## 2. Experimental Methods

The Ti-6Al-4V alloy investigated in this work was fabricated to the cylinder shaped parts as shown in Figure 2 from used grade 5 powder by an EB-PBF method, using an Arcam A2X machine (Arcam AB, Mölndal, Sweden) at the Institute of Metals, Technion, Israel. The chemical compositions of the powder used are shown in Table 1. The original powder compositions reported by the vendors are within the criteria which meet the ASTM requirements listed in reference [27]. The used powder and the as-built materials had the same high oxygen values (oxygen content exceeded ASTM F2924 standard requirements [27]). One layer of powder ( $\sim 70 \mu\text{m}$ ) was spread on a platform of a pre-heated plate. Each powder layer was pre-heated in order to attain a temperature between  $550 \text{ }^\circ\text{C}$  and  $700 \text{ }^\circ\text{C}$  ( $\sim 0.5 T_m$ , and  $T_m$  is the temperature of the melting point in Kelvin) by using a de-focused electron beam. Secondary pre-heating up to  $0.8 T_m$  selectively heated only the designated surface areas that were melted eventually by electron beam. Hence, the temperature of the entire build part during the AM process continuously varied within seconds between about  $700 \text{ }^\circ\text{C}$  at the current printed layer and about  $400 \text{ }^\circ\text{C}$  at the lowest (first) layer (note that this temperatures are estimates, as these temperatures were never measured to the best of our knowledge). By repeating the process, the full height of the product was fabricated. The acceleration voltage of the electron beam remained constant at 60 kV. Vacuum conditions were  $10^{-5}$  mbar of the initial vacuum with a needle valve regulating a constant  $10^{-3}$  mbar helium environment. The electron beam path and the parameters (e.g., beam speed and current) were guided by an algorithm (proprietary) formulated by Arcam. The purpose of this algorithm was to maintain a constant heat deposition ( $\text{J}/\text{mm}^2$ ) in each area in a single layer; additionally, all layers should have had a similar heat deposition. In the current work, the geometries were simple, and therefore, equal heat deposition was achievable in a cylindrical part. There is no texture difference as a function of distance from powder bed [13]. On the other hand, a microstructure difference upon location (build placement) was observed [27]. Mechanical properties of the as-built material as determined by tensile testing are shown in Table 2. Even with the large amount of oxygen, the EB-PBF material used in this study showed high elongation, possibly due to a fine microstructure characteristic of the EB-PBF method. More information was reported in our previous manuscripts [13,27].

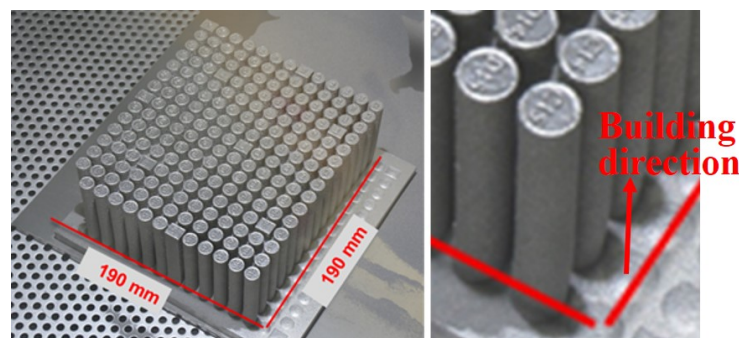


**Figure 2.** Ti-6Al-4V specimen fabricated by the EB-PBF process. The size of each rod sample is  $\phi 11 \text{ mm} \times 70 \text{ mm}$ .

**Table 1.** Chemical compositions of the Ti-6Al-4V powder (mass%).

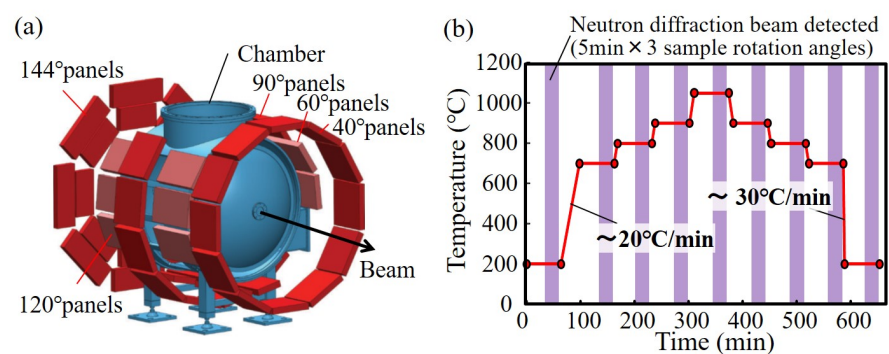
Element	Al	V	O	C	H	Fe	Ti
Original powder (ASTM F2924)	5.50– 6.75	3.5– 4.5	<0.2	<0.08	<0.0015	<0.3	Balance
Used powder	6.5 $\pm 0.13$	3.86 $\pm 0.04$	0.34 $\pm 0.01$	0.031 $\pm 0.001$	0.0027 $\pm 0.0008$	0.27 $\pm 0.05$	89.0 $\pm 0.22$

**Table 2.** Tensile properties of as-built material [27].

Properties	Young's Modulus /GPa	Proof Stress $R_{p0.2}$ /MPa	Tensile Strength /MPa	Elongation /%	Reduction of Area /%	Number of Materials
ASTM F2914 requirements		min.825	min.895	min.10	min.15	
Average and standard deviation	118.8 ± 3.8	1036 ± 17	1122 ± 22	9.8 ± 3.8	11.5 ± 5.6	12

### 2.1. Neutron Diffraction

One of the rod pillar samples cut from the product was used for a bulk analysis, using HIPPO (high pressure preferred orientation time-of-flight diffractometer) at the pulsed LANSCE (Los Alamos Neutron Science Center) neutron source [28,29]. Diffraction histograms were collected at different temperatures for a sample prepared from the middle part of a rod by exposing the sample to a neutron beam with a circular cross section of diameter of 10 mm for 20 min (Figure 3). The incident beam was parallel to the build direction of the sample. Diffraction histograms were analyzed by means of Rietveld analysis [30], using the MAUD software [31] to evaluate the phase fraction in weight percent, as well as the crystallographic texture following the procedures described in [32]. For the texture analysis, the orientation distribution function (ODF) was described by the E-WIMV algorithm in MAUD [32], using a resolution of 7.5 degrees. Diffraction histograms were obtained as a function of temperature starting at room temperature and heating up to 1050 °C, using a vanadium sample holder, vanadium heating elements and heat shields in the furnace. Vanadium has a negligible coherent neutron cross section and thus, does not contribute reflections to the measured diffraction histograms [13,29]. Vacuum conditions were  $10^{-6}$  torr. The sample was held at each temperature for about 60 min. Presumably due to an unstable microstructure during temperature equilibration, the histograms obtained at the early stage of temperature holding resulted in a poor Rietveld analysis. Therefore, only histograms from the last 15 min—5 min each at the three sample rotation angles of 0°, 67.5°, and 90°—were used (Figure 3b). The detailed procedure can be found in [13].

**Figure 3.** (a) The HIPPO diffractometer. (b) Heat pattern used in the present neutron diffraction experiment.

### 2.2. EBSD

Direct observation of microstructure evolution was carried out by the in situ heating EBSD measurement [33,34] with an FE-SEM (JSM-7001F, JEOL, Japan) operating at 15 kV of the accelerating voltage. A heating stage system (HSEA-1000, TSL Solutions Co., Ltd., Japan) was used, and the heating stage was mounted on a SEM sample stage. A sheet sample was cut from the middle part of an as-built rod sample by using wire electric discharge machining to the size of 5 mm × 7 mm × 1 mm (length × width × thickness). The thickness direction corresponds to the build direction. One surface of the sample was polished by a standard method with a final step, using 0.04 μm colloidal silica particles.

The temperature was measured by thermocouples attached to the surface of the sample as shown in Figure 4a.

Heat patterns used in the experiment are shown in Figure 4b. The heating rate was about  $2\text{ }^{\circ}\text{C/s}$ , which is about 8 times faster than the HIPPO experiment. The temperature changed in steps and the microstructure was scanned at each temperature. Once the temperature reached each target value, the EBSD pattern was obtained. Due to the thermal expansion, the sample moves inside the heating stage, especially when the temperature is changing. Therefore, before obtaining EBSD patterns, the sample position was adjusted, using a SEM sample stage, ensuring the observation area to be the same during the entire measurement.

The EBSD datasets were subjected to a clean-up procedure, using neighbor confidence index (CI) correlation with a minimum CI of 0.05, followed by a single iteration of grain dilation with a minimum grain size of 5 pixels for the in situ measurements and grain tolerance angle of  $5^{\circ}$ . After the clean-up process, misindexed data were replaced with the neighbor data that had a higher CI, and every data point was recognized as being part of a grain with a minimum grain size of the designated pixel numbers. The fraction of points changed in each data set was less than 2%. The EBSD data analysis was performed, using an OIM analysis software version 5.3.1 (EDAX Inc., Markham, ON, Canada). For the ex situ EBSD measurement before heating, an area of  $2000\text{ }\mu\text{m} \times 2000\text{ }\mu\text{m}$  was scanned with a step size of  $1.0\text{ }\mu\text{m}$ , and in the in situ measurement, an area of  $\sim 400\text{ }\mu\text{m} \times \sim 400\text{ }\mu\text{m}$  was scanned with a step size of  $0.4\text{ }\mu\text{m}$ . From the EBSD analysis, pole figures were constructed by a series expansion of generalized spherical harmonics, using smoothing parameters with Gaussian half-width of  $10^{\circ}$ , and plotted with an equal area projection method.

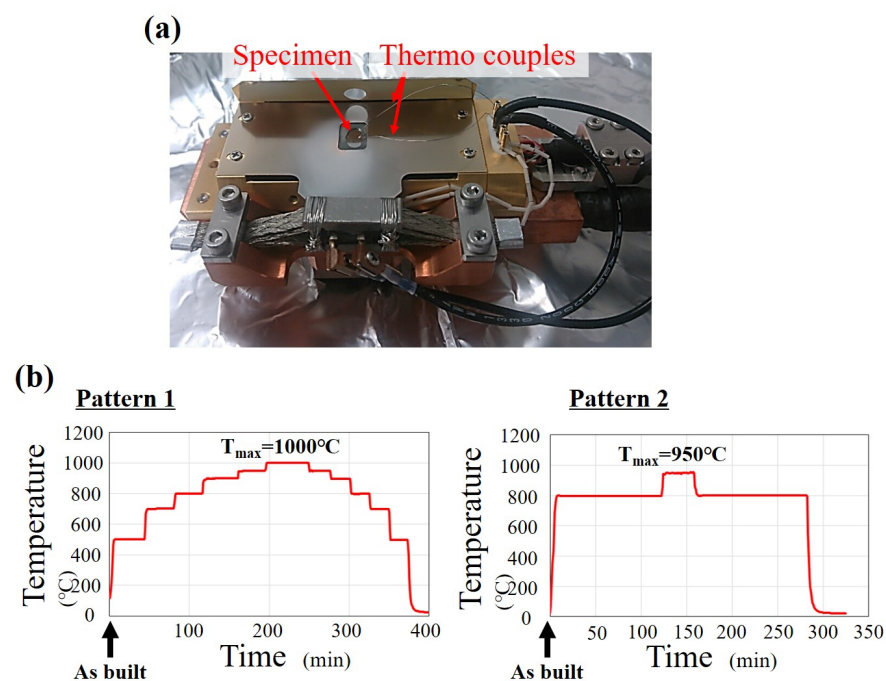


**Figure 4.** (a) Heating stage for SEM/EBSD. (b) Sample temperature as a function of time during SEM/EBSD measurement.

### 3. Model for Transformation Texture Formation

The texture transformation upon  $\alpha \rightarrow \beta \rightarrow \alpha$  phase transformation was modeled based on so-called double Burgers orientation relation (DBOR) as proposed in the literature [35]. In DBOR, the variants that satisfy BOR:  $\{0001\}_{\alpha} // \{011\}_{\beta}, < 11\bar{2}0 >_{\alpha} // < 111 >_{\beta}$  [36], in which there are 6 and 12 variants in  $\alpha \rightarrow \beta$  and  $\beta \rightarrow \alpha$  transformations, respectively, or relationship near to it (up to about 10 degrees of deviation allowed) preferentially nucleate and grow. Two types of growth modes were considered. One is that DBOR

variants nucleated on grain boundaries grow into the parent grain with which the variants hold BOR, and the growth is confined within the parent grain similar to the martensite transformation (see Figure 5a). The second mode is more extended in which the DBOR variants grow not only by the migration of the coherent interfaces, but also by semi-coherent or incoherent interfaces into the grains with which they hold only near-BOR or even no orientation relation (EDBOR) as shown in Figure 5b.

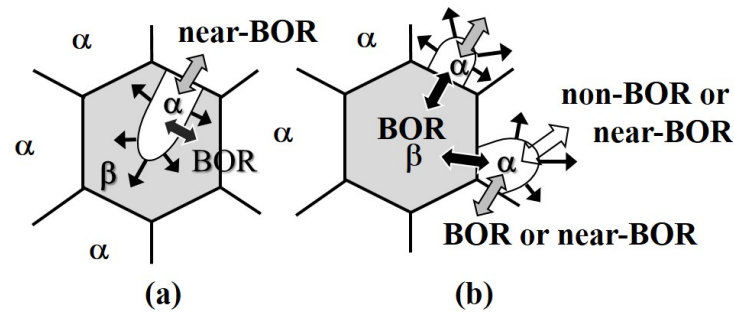


**Figure 5.** Schematic representations of nucleation and growth modes of DBOR variants. Growth of DBOR variants by (a) coherent interfaces and (b) semi-coherent or incoherent in  $\alpha \rightarrow \beta$  transformation.

The DBOR variants can appear on five and four kinds of special boundaries in  $\alpha$  and  $\beta$  parent grain structures, respectively, as listed in Table 3 [35]. Therefore, the probability for a particular variant to be chosen according to DBOR,  $\rho(g)$ , is related to the density of those special boundaries in the parent phase, where  $g$  specifies the orientation of a parent grain as well as the variant to be chosen. The  $\rho(g)$  is formulated for the former growth mode as follows:

$$\rho(g) = \frac{\omega}{N_k \times \bar{\zeta}} \sum_{k=1}^{N_k} \zeta_k \times f(\Delta g^{-1} \times g_k^c \times \Delta g \times g) + \rho_c(g) \quad (1)$$

$$\rho_c(g) = 1 - \frac{\omega}{N_i \times N_k \times \bar{\zeta}} \sum_{i=1}^{N_i} \sum_{k=1}^{N_k} \zeta_k \times f(\Delta g^{-1} \times g_k^c \times \Delta g \times g_i^p \times g) \quad (2)$$

**Table 3.** Special boundaries for DBOR.

Phase Transformation	Type	Rotation between Adjacent Grains			Number Ratio
		Angle	Axis	Deviation from $\langle 1\bar{2}10 \rangle$	
$\alpha \rightarrow \beta$	I	10.5°	c-axis	90°	1
	II	60°	$\langle 2\bar{1}\bar{1}0 \rangle$	0°	2
	III	60.8°	$\langle 7\bar{4}31 \rangle$	10.4°	4
	IV	63.3°	$\langle 4\bar{2}21 \rangle$	17.6°	2
	V	90°	$\langle 7\bar{4}30 \rangle$	5.3°	2
$\beta \rightarrow \alpha$	I	10.5°	$\langle 110 \rangle$	-	1
	II	49.5°	$\langle 110 \rangle$	-	1
	III	60°	$\langle 111 \rangle$	-	1
	IV	60°	$\langle 110 \rangle$	-	2

Here,  $f(g)$  is ODF of the parent phase,  $\Delta g$  is the crystal rotation due to BOR,  $g_k^c$  and  $g_i^p$  are rotational operators for crystal symmetry for child and parent crystals,  $N_k$  and  $N_i$  are the numbers of the operators (12 and 24 for  $\alpha$  and  $\beta$  phases), respectively. The first term in (1) is for the density of the special boundaries, and  $\zeta_k$  is the weight factor for each type of special boundaries, which is assumed to be unity in this study. The second term in (1),

$\rho_c(g)$  in (2), is the term for the growth mode. The parameter  $\omega$  is the strength parameter of the variant selection by DBOR, which is discussed below. Obviously when  $\omega$  is zero,  $\rho(g)$  is unity and the variant selection is absent. When  $\omega$  is unity,  $\rho_c(g)$  is close to zero and the nucleation and growth are all governed by the proposed DBOR mechanism. For the latter growth mode, EDBOR, the second term in (1),  $\rho_c(g)$  is replaced by a constant  $\delta$ , which is determined to maintain total volume of material during transformation [35]. In this study, the EDBOR calculation was used. The values of  $\zeta_k$  were chosen to be unity for  $\alpha \rightarrow \beta$  for simplicity. Those for  $\beta \rightarrow \alpha$  were chosen to be 0, 3, 1 and 1 for the I, II, III and IV types of the special boundaries that were determined for Ti in the previous study [35], respectively. The values of  $\zeta_k$  determined for  $\alpha \rightarrow \beta$  in the previous study were not used since they were thought to be influenced by macro-zones caused by rolling processes [35]. The  $\rho(g)$  in Equations (1) and (2) can be readily expanded by spherical harmonics [35], and the method for transformation texture calculation based on the harmonic expansion of ODF [37] can be used for the texture prediction. Therefore, the observed experimental textures measured on HIPPO were expanded by harmonics, using recalculated pole figures by MAUD, and the transformation textures were calculated using the DBOR model. In all calculations, the orthorhombic sample symmetry was applied in which the symmetry axes are along the c-axis direction and the normal direction in the initial pole figures. The harmonic expansion of the observed textures was performed, using a method described in the literature [38] for  $\alpha$  phase and the software called "standard ODF" [39] for  $\beta$  phase, which was truncated at the 28th and 22nd order for  $\alpha$  and  $\beta$ , respectively. The transformation texture calculation and the expansion of  $\rho(g)$  were truncated at the 20th and 28th orders, respectively.

## 4. Results and Discussion

### *Microstructure Evolution*

Selected regions of neutron diffraction histograms of Ti-6Al-4V measured at different temperature are shown in Figure 6a. The  $\beta$  phase reflection, {110}, is not readily visible at 200 °C in the heating process. With increasing temperature, this reflection clearly appears, shifts due to thermal expansion and the repartitioning of alloying elements, and grows in intensity due to an increasing weight fraction of the  $\beta$  phase. Contrary to that, the  $\alpha$  phase related reflections decrease with increasing temperature, until they vanish entirely at 1050 °C. Using the Rietveld analysis, we identified a hysteresis behavior of the  $\beta$  phase fraction and texture during the measurement heat cycle [13] as indicated by a small, but significant above the background, intensity of the  $\beta$  phase reflection {110} at 200 °C in the cooling process. Although it is almost zero before heat treatment, which is reasonable in light of thermodynamic equilibrium (Figure 1), the  $\beta$ -phase remains about 6% at room temperature after the heating and cooling cycle.

Texture analysis revealed an obvious enhancement of the hexagonal basal plane of  $\alpha$  phase {0001} parallel to the build direction after the heat cycle. Figure 6b shows changes in the maximum {0002} $_{\alpha}$  and {011} $_{\beta}$  pole density as a function of temperature. The pole density slightly decreases during the heating up to 900 °C at which the  $\alpha$  phase fraction is approximately 70% [13]. However, after it is retransformed from the full  $\beta$  phase in the cooling process, the  $\alpha$  phase exhibits a jump in the pole density. Besides that, the preferential orientation of {0001} along the build direction remains. This jump cannot be explained by a texture simulation where the variants are randomly selected, suggesting the presence of a variant selection mechanism as is well studied in the other materials [40].

Figure 7a shows inverse pole figure maps and phase maps during heat treatment analyzed by the EBSD method. The initial microstructure includes fine grains and partly shows the Widmanstätten structure. There is no obvious change in the microstructure during heating up to 800 °C, but the  $\beta$  phase increases at 900 °C and higher. Thousands of fine  $\alpha$  phase grains observed at room temperature transform to only several coarse  $\beta$  phase grains at 900 °C. Nucleation of the transformation is generally considered to occur near grain boundaries [41]. The high cooling rate of the AM process from the melt to the

temperature of the remaining part ( $\sim 700$  °C) would presumably increase the number of nucleations at the grain boundaries, explaining the observed fine  $\alpha$  microstructure.

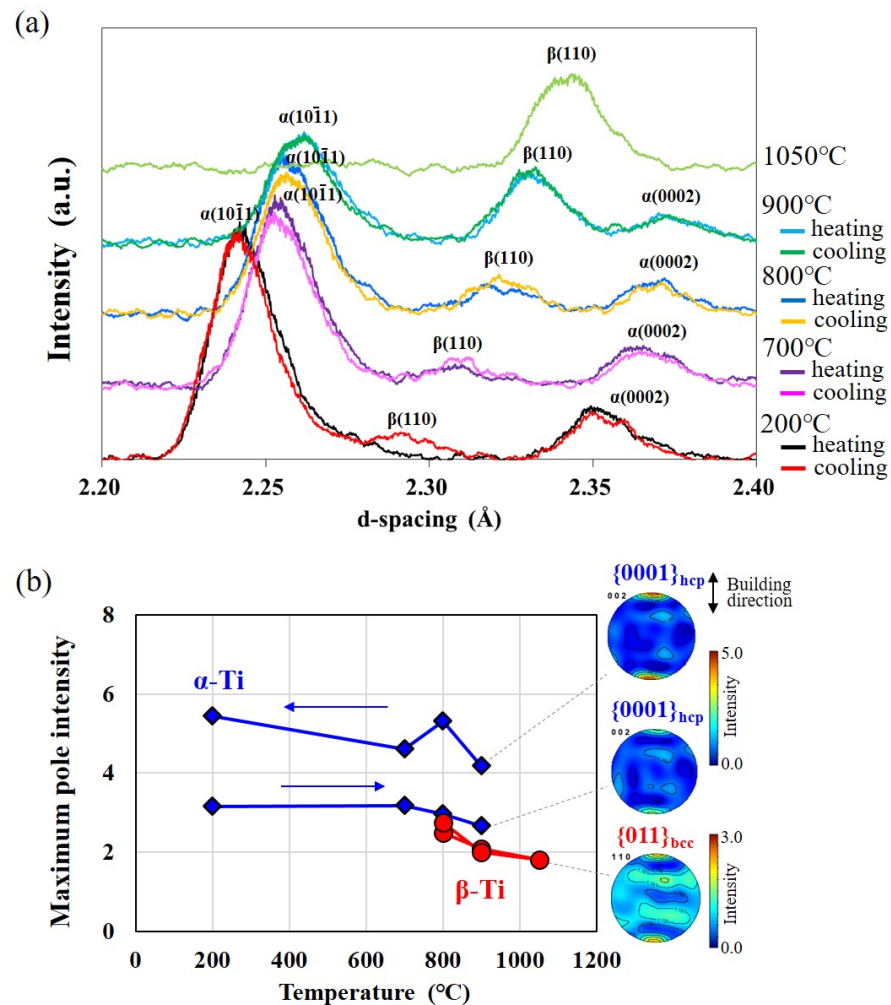


**Figure 6.** (a) Neutron time of flight diffraction spectra of Ti-6Al-4V measured at 200 °C, 700 °C, 800 °C, 900 °C and 1050 °C. (b) Changes in the maximum pole density as a function of temperature.

When the temperature reached 1000 °C, the microstructure consisted entirely of  $\beta$  phase. Furthermore, the grains at this stage grew excessively, resulting in only a single grain in the observed area as shown in Figure 7. During the cooling process, the  $\alpha$  phase fraction gradually increased with decreasing temperature, but the texture changed drastically after heat treatment (Figure 7b,c), unlike the neutron diffraction data [13]. This is due to the local characterization of the EBSD method, resulting for large-grained materials in poor grain statistics for texture characterization, much different from the bulk and averaging characterization by neutron diffraction, providing much better grain statistics, even for large-grained materials as is the case here. The significant grain growth of the  $\beta$  phase, together with the fact that the observed grain has a free surface where the EBSD is applied, precludes observation of  $\beta$  grain boundaries in the observed area such that the texture memory (of the previously observed  $\alpha$ ) did not occur in the field of view of the EBSD instrument. Thus, the texture memory could not be observed in the EBSD analysis. It should be noted that the bulk texture of  $\beta$  phase will not change significantly by the normal grain growth and, therefore, the bulk texture of  $\alpha$  phase did not change drastically (but slightly changed) as shown in the neutron diffraction data [13].

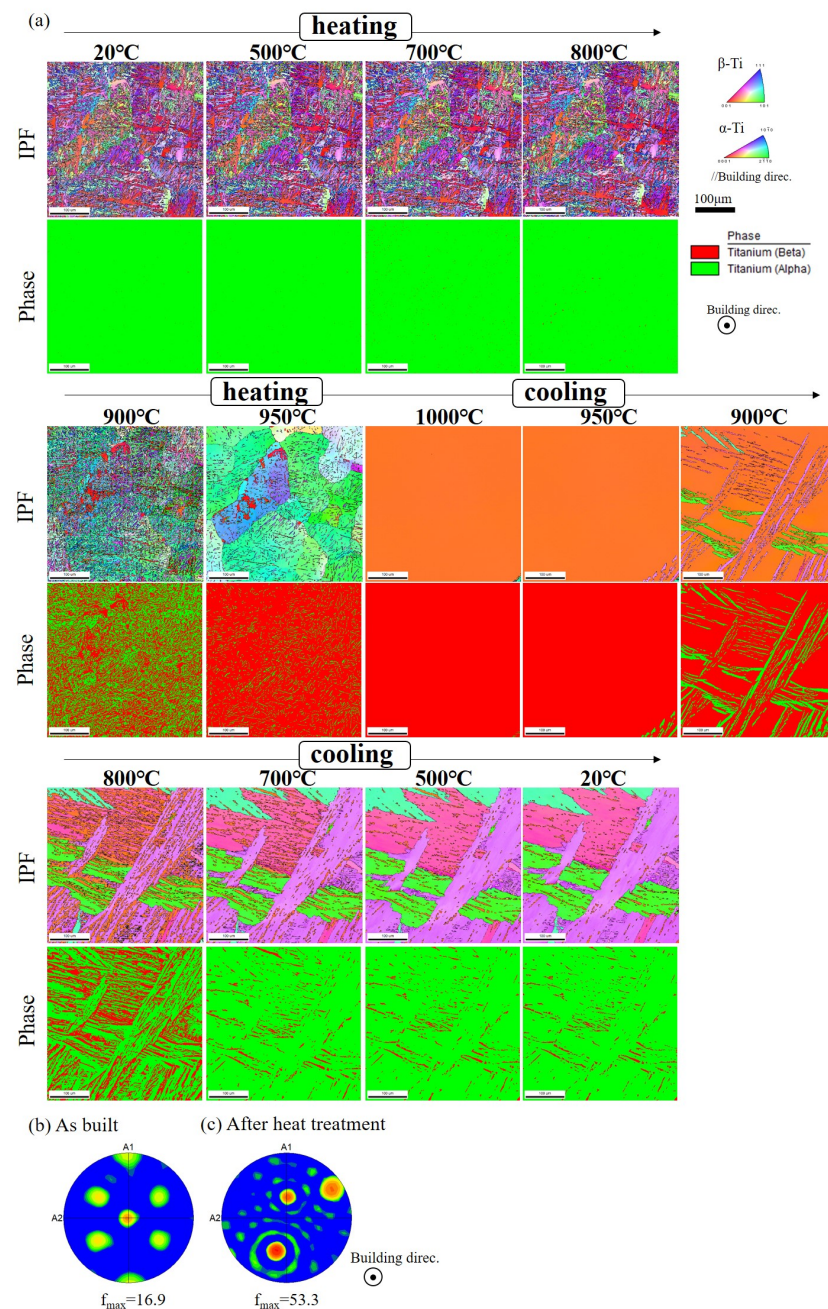


**Figure 7.** (a) Changes in inverse pole figure maps and phase maps during heat treatment. (b,c)  $\{10\bar{1}0\}$  pole figures of  $\alpha$ -Ti at room temperature before (b) and after (c) heat treatment determined by EBSD.

Figure 8 shows the changes in the phase fraction in volume as a function of temperature as measured by EBSD. A small amount of  $\beta$  phase  $\sim 0.5\%$  was detected before heat treatment, which was also reported in reference [42]. The irreversible response of crystallographic phase appears as shown at 950 °C. After cooling to room temperature,  $\sim 5\%$  of the  $\beta$  phase grains were retained, which is consistent with the neutron diffraction data.

The first EBSD measurement revealed that the prior  $\beta$  grain boundary did not change significantly up to 950 °C. Therefore, to investigate the possible texture memory of the  $\alpha$  phase during heat treatment, the second heat pattern with the maximum temperature of 950 °C (Figure 4b) was applied to the material, thus avoiding complete transformation to the  $\beta$  phase. Figure 9a shows the inverse pole figure maps and phase maps obtained in the second heat treatment. There is no indication of movement of  $\beta$  grain boundary at 950 °C.

Due to texture memory following the BOR, the original  $\beta$  grain formed at high temperature in the AM process is assumed to be reconstructed. The microstructure after heat treatment in this second heating experiment below the  $\alpha/\beta$  transus is similar to that before heat treatment but has a slight (but an important) difference as discussed below. About the same amount of  $\beta$  phase  $\sim 5\%$  remains after heat treatment as the material exposed to the first heat treatment crosses the  $\alpha/\beta$  transus, which is equivalent to the value investigated in the previous experiment [13].

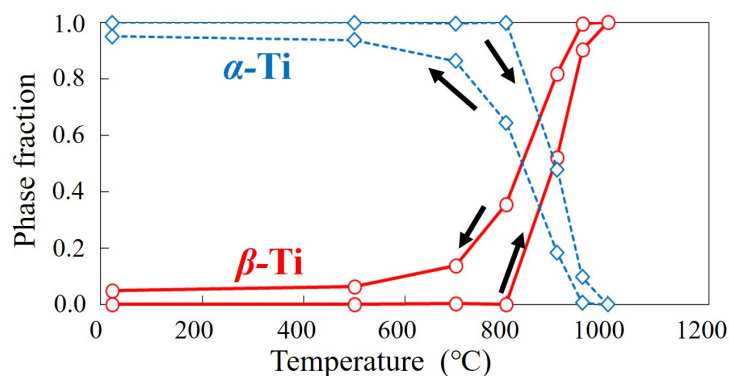


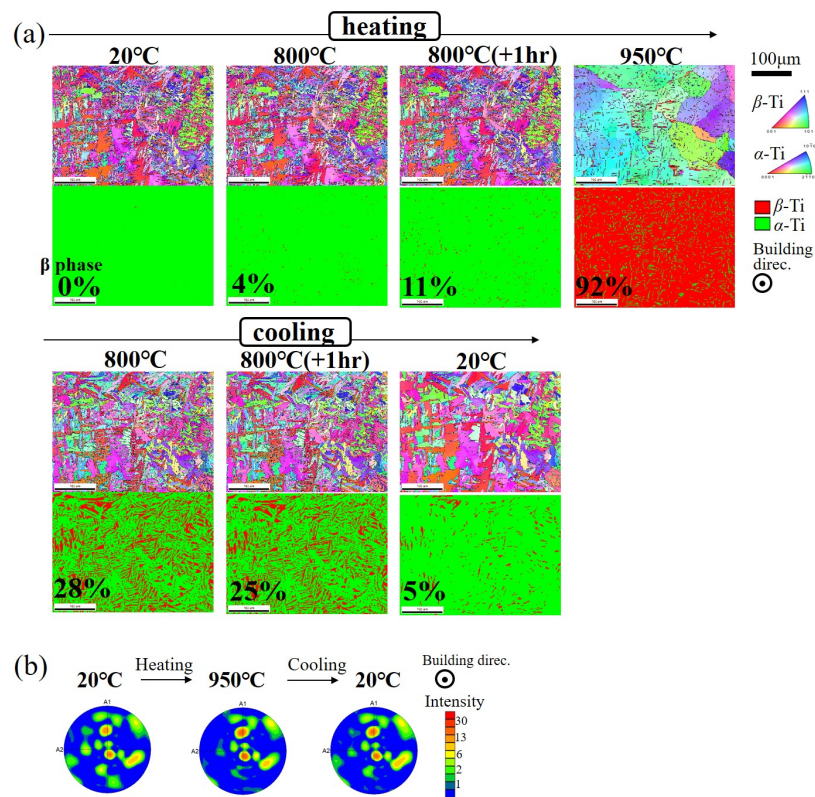
Figure 8. Changes in the phase fraction in volume as a function of temperature analyzed by EBSD method.

Figure 9b shows the  $\{10\bar{1}0\}$  pole figures of the  $\alpha$  phase. Texture does not change drastically after heat treatment, suggesting an effect of texture memory. However, the  $\alpha$  phase texture at 950 °C shows a slightly higher intensity than before heating, which remains, even after cooling.

Figure 10 shows elements distributions before and after heat treatment without crossing the  $\alpha/\beta$  transus analyzed by EPMA. As reported before [43,44], the concentration of elements V and Al is obviously enhanced in some regions after heat treatment in addition to the observation that some regions are depleted of Ti. Regions belonging to  $\beta$  Ti with b.c.c. crystal structure show lower Ti density than  $\alpha$  Ti with h.c.p. crystal structure. In regions where V is concentrated and both Al and Ti concentrations are decreased, the  $\beta$  phase is stabilized and hard to be transformed to the  $\alpha$  phase during cooling process. The increased  $\beta$  phase fraction after the heat treatment compared to the as-built material is therefore explained by elemental repartitioning. As studied in a forged material [45], exposure to high temperature around the  $\alpha/\beta$  transus followed by slow cooling allows the V to stabilize the  $\beta$  phase and leads to the hysteresis behavior of the phase fraction during heat treatment. In the EB-PBF process, on the other hand, the as-built material is pre-heated to  $\sim 700$  °C only for seconds, which is insufficient for the V to diffuse and stabilize the  $\beta$  phase. Our previous data [13] revealed that the lattice parameter of the  $\beta$  starts to deviate from the low temperature behavior at  $\sim 600$  °C, indicating that in addition to thermal expansion, lattice parameter changes due to vanadium redistribution occur. Our findings suggest, therefore, that vanadium redistribution, enabling the stabilization of the  $\beta$  phase, only occurs at temperatures higher than at least 600 °C.

Previous studies reported that the cooling rate influences the resulting microstructure during the  $\beta$  to  $\alpha$  phase transformation [12,45–47]. Reference [19] reported that the martensitic phase appears with the cooling rate 410 °C/s and more, while another work indicated that the martensitic phase decomposes into  $\alpha + \beta$  in the EB-PBF process [48], even with an estimate that the cooling rate in the EB-PBF process is much faster than 410 °C/s [12]. Wang et al. [49] showed that the scanning speed of the electron beam during the build affects the microstructure and that the martensitic phase  $\alpha'$  exhibits fine microstructure  $\sim 3$   $\mu\text{m}$ . Figure 11 shows the build direction (BD) inverse pole figure map of an AM fabricated sample. The microstructure shows the basket weave morphology. The average minor axis size of grain is  $1.30 \pm 1.56$   $\mu\text{m}$ , which is approximately the same as an AM fabricated sample reported in reference [47]. However, the electron beam AM material used in this study exhibits a mixture of large  $\alpha$  colony phase and small grains as shown in the upper

area of the figure. We assume that the fine microstructure corresponds to the martensitic  $\alpha'$  phase.



**Figure 9.** (a) Changes in inverse pole figure maps (**upper**) and phase maps (**lower**). The black lines in the inverse pole figure indicate the grain boundaries with the misorientation angle of 15° or more. (b) Changes in  $\{10\bar{1}0\}$  pole figure of  $\alpha$  phase measured using EBSD.

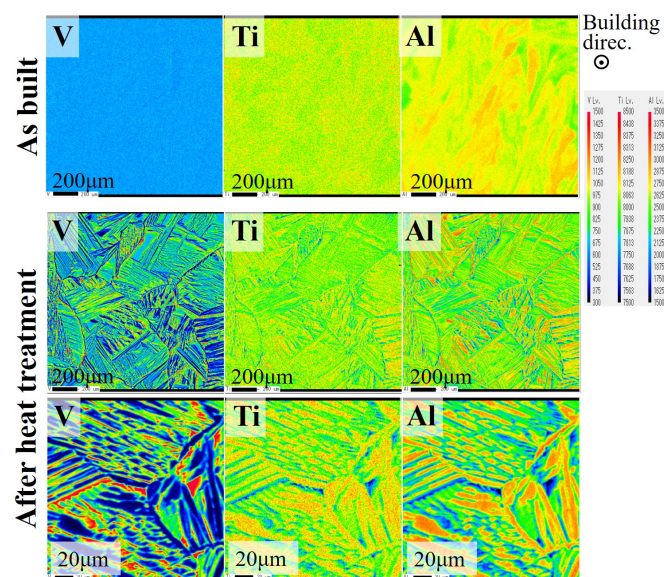


**Figure 10.** EPMA analysis of major elements before (**upper**) and after (**middle and lower**) heat treatment Pattern 2.

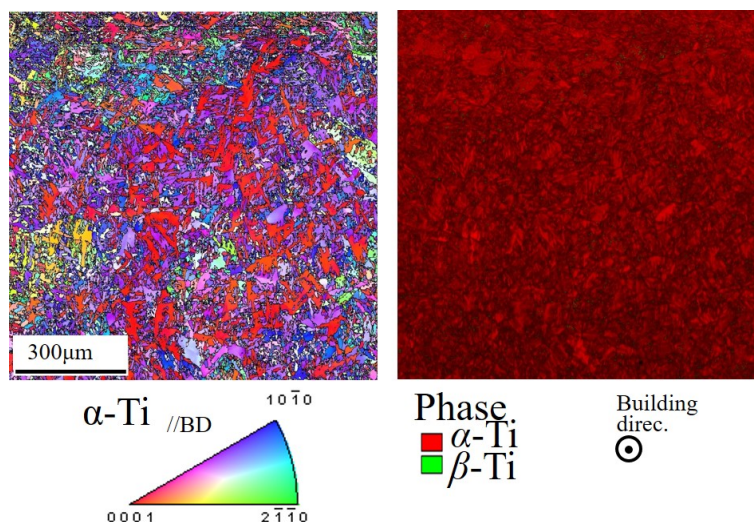


Figure 11. Build direction (BD) inverse pole figure map and phase map of the as-built material.

The cooling rate in the heating experiment in this study is about 4 °C/s (from 750 °C to 300 °C) and, therefore, is much lower than in the EB-PBF process, where the martensitic phase does not occur. A careful inspection of the inverse pole figure map (Figure 9a) revealed that fine  $\alpha$  grains found in the as-built sample disappear after the transformation from  $\beta$  phase, leading to a more homogeneous and larger grain size of the  $\alpha$  phase as shown in Figure 12a.

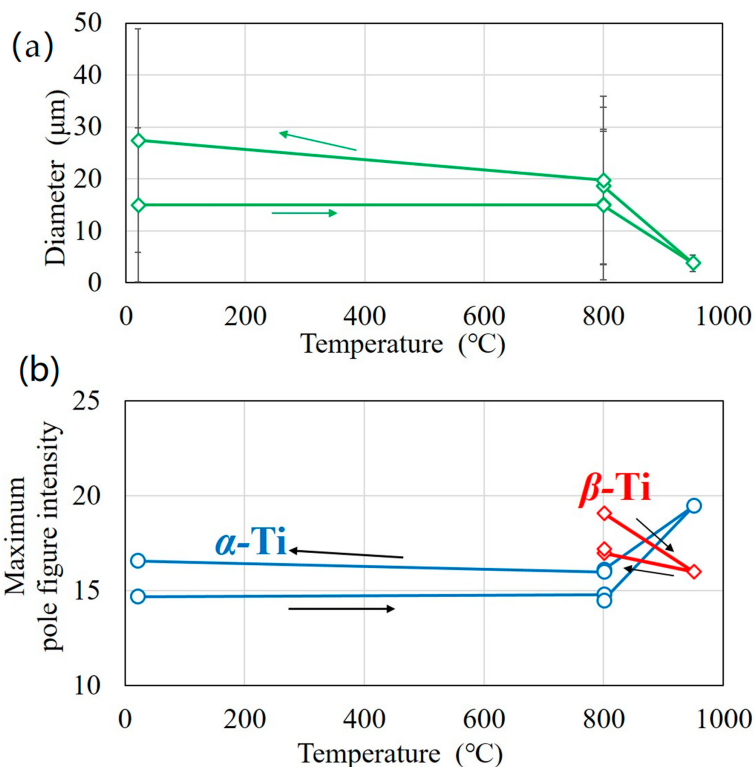
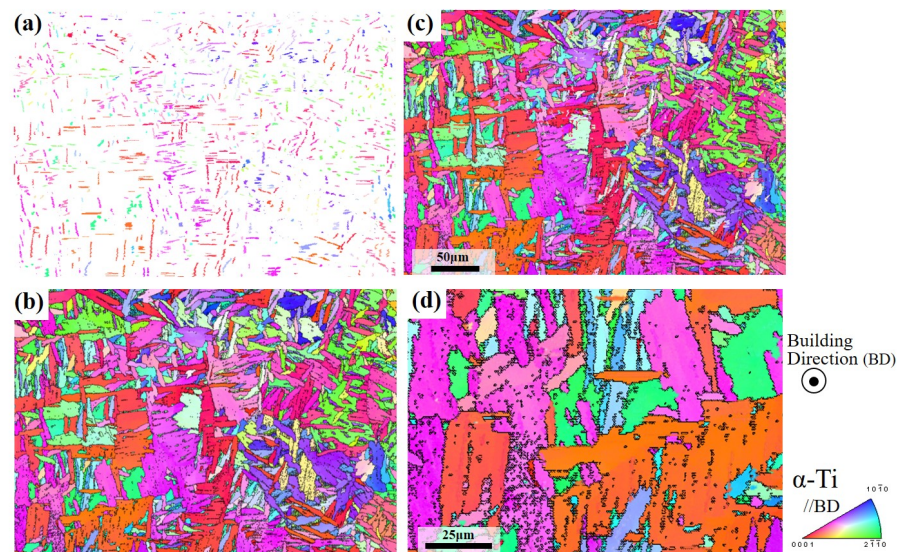


Figure 12. (a) Grain diameter and (b) {0002} pole density of  $\alpha$  phase obtained by EBSD analysis.

Figure 13 shows the grain map relationship of  $\alpha$  phase between 950 °C and 20 °C analyzed in the same observation area. In the figures, the  $\alpha$  phase grains at 20 °C are recognized by grain boundaries as indicated by the black line, while grains are shown without boundaries at 950 °C. The superimposed maps of Figure 13a,b are shown in Figure 13c,d. The figures are not perfectly superimposed with each other due to thermal expansion

during the EBSD measurement, but it is clear from the enlarged view in Figure 13d that there is little orientation deviation inside each grain of 20 °C, suggesting that the  $\alpha$  grains observed at 950 °C are a part of  $\alpha$  grains of 20 °C and that the increase in the  $\alpha$  phase fraction during cooling derives from the grain growth of existing  $\alpha$  phase rather than the nucleation of new  $\alpha$  grains.

The maximum {0002} pole figure density in Figure 12 suggests that the texture during the grain growth of the cooling process from 800 °C to 20 °C does not change significantly. The slight increase in the {0002} pole density of the  $\alpha$  phase likely derives from grain growth during the heating process or  $\beta$  to  $\alpha$  transformation at the higher temperature.



**Figure 13.** (a) Inverse pole figure of  $\alpha$  phase at 950 °C. (b) Inverse pole figure of  $\alpha$  and  $\beta$  phases at 20 °C with black line of the grain boundaries, (c) superimposed map of (a,b,d) enlarged view of (c). The black lines in the inverse pole figure indicate the grain boundaries with the misorientation angle of 5° or more.

To analyze the texture in detail, the microstructure of an AM fabricated sample was divided into two groups: an area with large grains ( $>5 \mu\text{m}$ ) and the other area with small grains ( $\leq 5 \mu\text{m}$ ). The texture of each microstructure was investigated, using OIM analysis. The area fraction of the grains with dimension 5  $\mu\text{m}$  and less, which we consider the martensitic phase, was 9.2%. Figure 14 shows the inverse pole figure maps and corresponding pole figures. The microstructure with large grains shows much higher {0002} pole density along the build direction than that with small grains. Given that the small grains in the AM processed sample are the martensitic phase, they exhibit a random texture due to the large number of  $\alpha'$  variants from the  $\beta$  phase. The small grains shrink easily in the process of grain growth to reduce the boundary energy in the system. Therefore, the  $\alpha'$  grains are consumed by grain growth in the process of the heating, which leads to texture enhancement as shown in Figure 12b. During the cooling process, new  $\alpha'$  grains are not generated, due to the low cooling rate as discussed above and, thus, the strong texture remains during the cooling process.

However, the mechanism of the texture enhancement of  $\alpha$  phase transformed from 100%  $\beta$  phase as measured in our neutron diffraction study is still not understood. In fact, the degree of the texture enhancement of  $\alpha$  phase after heat treatment is much larger when the microstructure is exposed to full  $\beta$  (Figure 6b) rather than  $\alpha$  and  $\beta$  dual phase temperature regions during heat treatment (Figure 12). Unlike the EBSD measurement with the second heat treatment not crossing the  $\alpha/\beta$  transus above, the nucleation of the  $\alpha$  phase after full transformation to  $\beta$  occurs inevitably in the cooling process from full  $\beta$  phase to increase the phase fraction. In what follows, we apply the new transformation model with the double Burgers orientation relationship (DBOR) to address the texture

evolution in the  $\alpha \rightarrow \beta \rightarrow \alpha$  phase transformation to explain the observed strengthening of the texture.

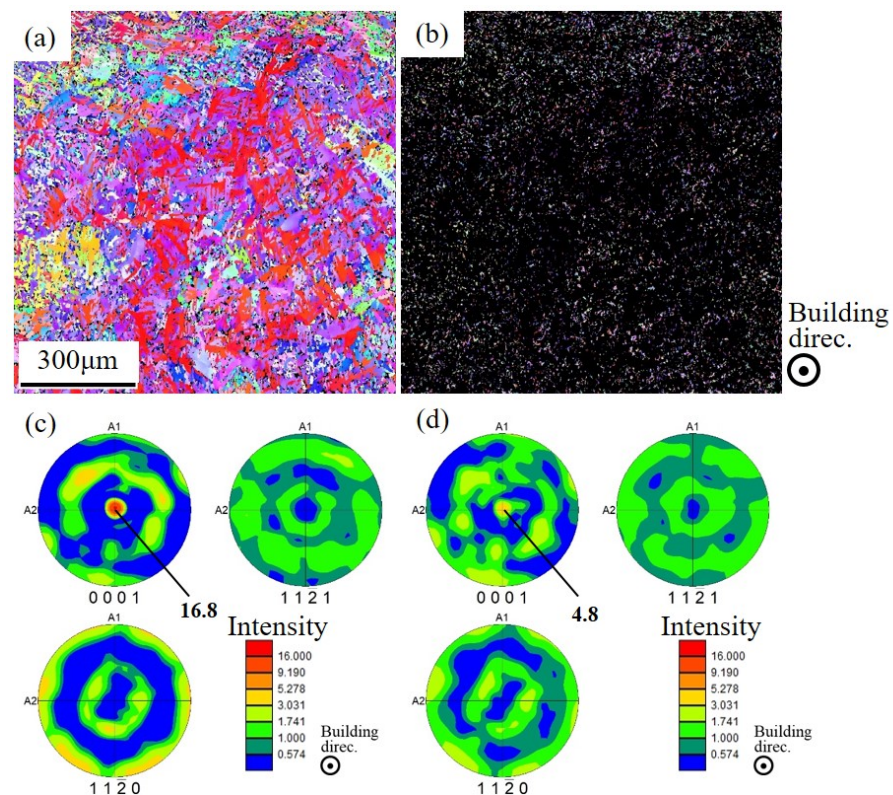


**Figure 14.** Inverse pole figure maps of as fabricated sample: (a) grain size  $>5 \mu\text{m}$  (b)  $\leq 5 \mu\text{m}$ . (c,d) Corresponding pole figures of (a,b), respectively.

The results of transformation texture prediction by using the observed parent textures and EDBOR are shown as pole figures and cross-sections of ODF in Figures 15 and 16, respectively. Note that the predicted  $\beta$  textures were used to calculate the final  $\alpha$  textures. The values of  $\omega$  in Equation (1) were determined to be 0.15 and 1.5 for  $\alpha \rightarrow \beta$  and  $\beta \rightarrow \alpha$  transformations by minimization of root mean square deviation between ODFs of predicted and observed child textures. The agreement between the predicted and observed textures of high temperature  $\beta$  and final  $\alpha$  is excellent. This suggests that (1) the phase transformations for not only  $\beta \rightarrow \alpha$ , but also  $\alpha \rightarrow \beta$  should be caused by nucleation and growth of child phases (not by growth of residual child phases), (2) the nucleation takes place on grain boundaries of parent phases and the variants are at least partly selected to reduce the interfacial energy, having BOR or near-BOR with multiple parent grains, and (3) whereas the variant selection for  $\alpha \rightarrow \beta$  is weak, that for  $\beta \rightarrow \alpha$  is rather strong in the AM material studied here, which is different from the behavior observed in rolled Ti [35]. The smaller value of  $\omega$ , 0.15 for  $\alpha \rightarrow \beta$ , suggests that the nucleation should occur without variant selection on general grain boundaries that are not the special boundaries for DBOR. As described in the previous research [35], the probability for the DBOR variants to be available on the plane grain boundaries in texture-less materials is only about 13% for  $\alpha \rightarrow \beta$  transformation, when angular deviation up to  $10^\circ$  is allowed for BOR on one side of the grain boundary. Although textures can alter the probability, the observed texture of  $\alpha$  is relatively weak and, more importantly, the main texture component is of a c-axis fiber, in which only the type I special boundary is allowed; the other types of special boundaries have rotation axes near  $\langle 12\bar{1}0 \rangle$  (see Table 3). Nucleation on triple junctions or grain corners can increase this probability by twice or more. However, there are still many parent grains in which no DBOR variant is available on surrounding boundaries; then, non-DBOR variants nucleate instead. Therefore, the value of  $\omega$  should be much

smaller than unity as predicted. For  $\beta \rightarrow \alpha$ , the above probability for DBOR variants in textureless materials is larger and 19% on plane boundaries. Furthermore, whereas the observed texture of  $\beta$  is not strong either, it is of a  $\langle 110 \rangle$  fiber in that the types I, II and IV of special boundaries for DBOR are allowed. The probability thus significantly increases so that an ideal DBOR variant selection should be statistically possible. Hence, the texture memory upon  $\alpha \rightarrow \beta \rightarrow \alpha$  phase transformation in the present AM material can be well explained by the DBOR mechanism.

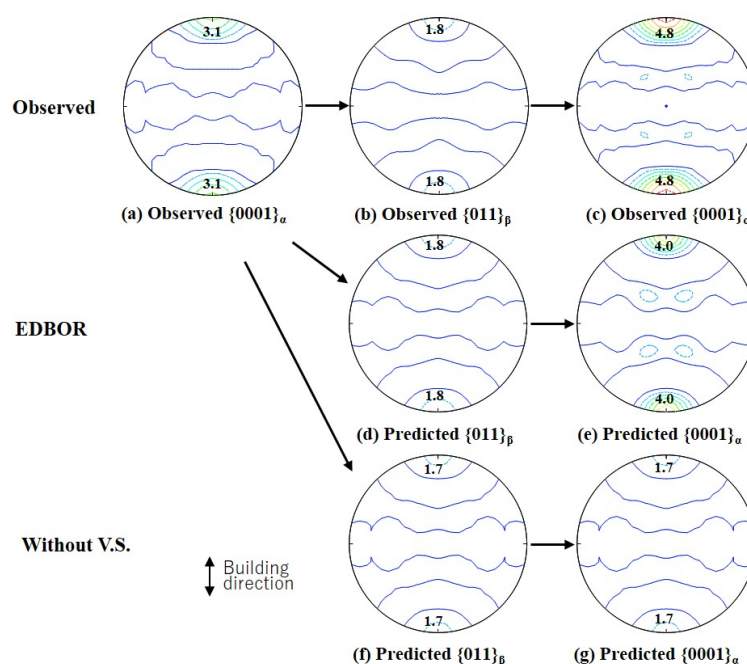


**Figure 15.** (a–c) Observed pole figures at (a) 900 °C before transformation, (b) 1050 °C and (c) 900 °C after transformation, (d–g) predicted pole figures based on (d,e) DBOR mechanisms and (f,g) without variant selection. Levels are 1.0, 1.5, 2.0, 2.5...

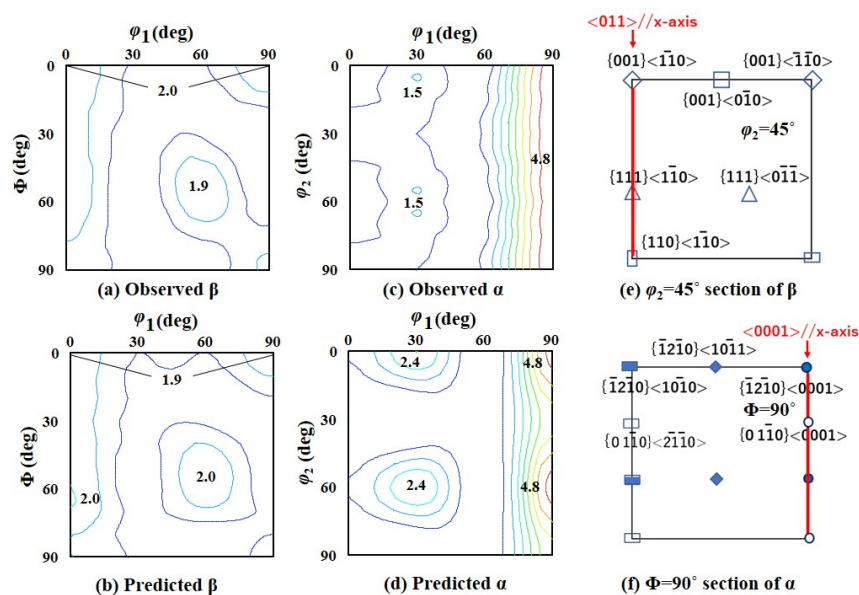


**Figure 16.** ODF sections of (a,c) observed textures of (a)  $\beta$  at 1050 °C and (c) final  $\alpha$  at 900 °C and (b,d) predicted textures of (b)  $\beta$  and (d) final  $\alpha$ . (e,f) Important orientations. Contour levels are 1, 1.5, 2, 3.5...

## 5. Conclusions

The microstructure evolution of an additively manufactured Ti-6Al-4V during heat treatment was explored by means of in situ EBSD, complementing data from high temperature in situ neutron diffraction. An enhancement of the  $\alpha$  phase texture and an increase in the phase fraction of  $\beta$  phase after heat treatment were observed in the EBSD experiment, although the degree of enhancement of the  $\alpha$  texture was smaller than the bulk analysis, using neutron diffraction. However, this deviation can be explained by the poor grain statistics of the EBSD technique. Due to the advantage in grain level analysis, the EBSD analysis plus EPMA revealed the following new outcome.

(i) The rapid solidification phenomena, which is a typical AM powder bed outcome, dictates a unique fine microstructure in as-built material. A heating cycle, analyzed utilizing EBSD, reveals that the smaller  $\alpha$  grains, which exhibit a weak texture, disappear in the early stage of heating, while the relatively large  $\alpha$  grains remain at high temperature. Even after cooling from 950 °C, most of the  $\alpha$  grains remain and coarsen by grain growth, while fine  $\alpha$  grains as shown in the as-built material are not frequently observed possibly due to a slow cooling rate. Thus, the  $\alpha$  phase texture develops slightly after a heat treatment with the maximum temperature of 950 °C, where several percentages of  $\alpha$  phase remain.

(ii) Vanadium concentrates in the  $\beta$  phase after heat treatment, which is not observed in the as-built material. The slow cooling in the heat cycle is considered to allow for the vanadium atoms to diffuse and stabilize the  $\beta$  phase, leading to a suppression of  $\alpha$  nucleation and a few weight percentage points of the retained  $\beta$  phase at room temperature.

Furthermore, the texture simulation that follows the double Burgers orientation relationship successfully reproduced the experimentally observed texture enhancement of the  $\alpha$  phase after transformation from the full  $\beta$  phase at 1050 °C as analyzed from the neutron diffraction experiment. This suggests that the variant selection at the grain boundary as well as the transformation from the 100%  $\beta$  phase is a key to the preferential  $\alpha$  texture formation.

**Author Contributions:** Conceptualization, S.T. and S.C.V.; methodology, S.T., E.T., T.T. and S.C.V.; software, S.T., S.C.V. and T.T.; validation, E.N.C. and A.P.; formal analysis, S.T., E.T. and S.C.V.; investigation, S.T. and S.C.V.; resources, S.T., E.T., A.P. and S.C.V.; data curation, E.N.C. and S.C.V.; writing—original draft preparation, S.T. and T.T.; writing—review and editing, S.T., E.N.C., E.T. and S.C.V.; visualization, S.T.; supervision, S.C.V.; project administration, S.C.V.; funding acquisition, S.C.V. and E.T. All authors have read and agreed to the published version of the manuscript.

**Funding:** The authors are grateful to Pazy Foundation for its partial support of the present study (grant 2020-ID147). This work was performed under the auspices of the National Nuclear Security Administration-Israel Atomic Energy Commission Memorandum of Understanding for science cooperation. And The APC was funded by S.C.V. (LANL).

**Acknowledgments:** The authors gratefully acknowledge the sample fabrication by Max Shrager, Institute of Metals, Technion. This work has benefited from the use of the Los Alamos Neutron Science Center (LANSCE) at LANL. Los Alamos National Laboratory is operated by Triad National Security, LLC, for the National Nuclear Security Administration of the U.S. Department of Energy under contract number 89233218NCA000001.

**Conflicts of Interest:** The authors declare no conflict of interest.

## References

1. Flower, H. Metal-based composite materials. In *High Performance Materials in Aerospace*; Springer: Berlin/Heidelberg, Germany, 1995; pp. 227–245.
2. Tomlin, M.; Meyer, J. Topology optimization of an additive layer manufactured (ALM) aerospace part. In *Proceeding of the 7th Altair CAE Technology Conference*, Gaydon, UK, 10–12 May 2011; pp. 1–9.
3. Olakanmi, E.; Cochrane, R.; Dalgarno, K. Progress in materials science a review on selective laser sintering/melting (SLS/SLM) of aluminium alloy powders: Processing, microstructure, and properties. *J. Prog. Mater. Sci.* **2015**, *74*, 401–477. [[CrossRef](#)]
4. Liu, S.; Shin, Y.C. Additive manufacturing of Ti6Al4V alloy: A review. *Mater. Des.* **2019**, *164*, 107552. [[CrossRef](#)]
5. de Formanoir, C.; Michotte, S.; Rigo, O.; Germain, L.; Godet, S. Electron beam melted Ti-6Al-4V: Microstructure, texture and mechanical behavior of the as-built and heat-treated material. *Mater. Sci. Eng. A* **2016**, *652*, 105–119. [[CrossRef](#)]

6. Tan, X.; Kok, Y.; Toh, W.Q.; Tan, Y.J.; Descoins, M.; Mangelinck, D.; Tor, S.B.; Leong, K.F.; Chua, C.K. Revealing martensitic transformation and  $\alpha/\beta$  interface evolution in electron beam melting three-dimensional-printed Ti-6Al-4V. *Sci. Rep.* **2016**, *6*, 1–10. [[CrossRef](#)] [[PubMed](#)]
7. Tan, X.; Kok, Y.; Tan, Y.J.; Vastola, G.; Pei, Q.X.; Zhang, G.; Zhang, Y.W.; Tor, S.B.; Leong, K.F.; Chua, C.K. An experimental and simulation study on build thickness dependent microstructure for electron beam melted Ti-6Al-4V. *J. Alloys Compd.* **2015**, *646*, 303–309. [[CrossRef](#)]
8. Pesach, A.; Tiferet, E.; Vogel, S.C.; Chonin, M.; Diskin, A.; Zilberman, L.; Rivin, O.; Yehekel, O.; El'ad, N.C. Texture analysis of additively manufactured Ti-6Al-4V using neutron diffraction. *Addit. Manuf.* **2018**, *23*, 394–401. [[CrossRef](#)]
9. Bhattacharyya, D.; Viswanathan, G.; Vogel, S.; Williams, D.; Venkatesh, V.; Fraser, H. A study of the mechanism of  $\alpha$  to  $\beta$  phase transformation by tracking texture evolution with temperature in Ti-6Al-4V using neutron diffraction. *Scr. Mater.* **2006**, *54*, 231–236. [[CrossRef](#)]
10. Lonardelli, I.; Gey, N.; Wenk, H.R.; Humbert, M.; Vogel, S.; Lutterotti, L. In situ observation of texture evolution during  $\alpha \rightarrow \beta$  and  $\beta \rightarrow \alpha$  phase transformations in titanium alloys investigated by neutron diffraction. *Acta Mater.* **2007**, *55*, 5718–5727. [[CrossRef](#)]
11. Sundman, B.; Jansson, B.; Andersson, J.O. The thermo-calc databank system. *Calphad* **1985**, *9*, 153–190. [[CrossRef](#)]
12. Al-Bermani, S.; Blackmore, M.; Zhang, W.; Todd, I. The origin of microstructural diversity, texture, and mechanical properties in electron beam melted Ti-6Al-4V. *Metall. Mater. Trans. A* **2010**, *41*, 3422–3434. [[CrossRef](#)]
13. Vogel, S.; Takajo, S.; Kumar, M.; Caspi, E.; Pesach, A.; Tiferet, E.; Yehekel, O. Ambient and High-Temperature Bulk Characterization of Additively Manufactured Ti-6Al-4V Using Neutron Diffraction. *JOM* **2018**, *70*, 1714–1722. [[CrossRef](#)]
14. Semiatin, S.; Levkulich, N.; Tiley, J. Effect of Cooling Rate on Microstructure Evolution and Plastic Flow of Ti-6Al-4V. *Metall. Mater. Trans. A* **2021**, *52*, 2238–2260. [[CrossRef](#)]
15. Semiatin, S.; Knisley, S.; Fagin, P.; Barker, D.; Zhang, F. Microstructure evolution during alpha-beta heat treatment of Ti-6Al-4V. *Metall. Mater. Trans. A* **2003**, *34*, 2377–2386. [[CrossRef](#)]
16. Ter Haar, G.M.; Becker, T.H. Selective laser melting produced Ti-6Al-4V: Post-process heat treatments to achieve superior tensile properties. *Materials* **2018**, *11*, 146. [[CrossRef](#)] [[PubMed](#)]
17. Chong, Y.; Bhattacharjee, T.; Tsuji, N. Bi-lamellar microstructure in Ti-6Al-4V: Microstructure evolution and mechanical properties. *Mater. Sci. Eng. A* **2019**, *762*, 138077. [[CrossRef](#)]
18. Jovanović, M.T.; Tadić, S.; Zec, S.; Mišković, Z.; Bobić, I. The effect of annealing temperatures and cooling rates on microstructure and mechanical properties of investment cast Ti-6Al-4V alloy. *Mater. Des.* **2006**, *27*, 192–199. [[CrossRef](#)]
19. Ahmed, T.; Rack, H. Phase transformations during cooling in  $\alpha + \beta$  titanium alloys. *Mater. Sci. Eng. A* **1998**, *243*, 206–211. [[CrossRef](#)]
20. Katzarov, I.; Malinov, S.; Sha, W. Finite element modeling of the morphology of  $\beta$  to  $\alpha$  phase transformation in Ti-6Al-4V alloy. *Metall. Mater. Trans. A* **2002**, *33*, 1027–1040. [[CrossRef](#)]
21. Obasi, G.; Biroasca, S.; Prakash, D.L.; Da Fonseca, J.Q.; Preuss, M. The influence of rolling temperature on texture evolution and variant selection during  $\alpha \rightarrow \beta \rightarrow \alpha$  phase transformation in Ti-6Al-4V. *Acta Mater.* **2012**, *60*, 6013–6024. [[CrossRef](#)]
22. Gey, N.; Humbert, M.; Philippe, M.; Combres, Y. Investigation of the  $\alpha$ - and  $\beta$ -texture evolution of hot rolled Ti-64 products. *Mater. Sci. Eng. A* **1996**, *219*, 80–88. [[CrossRef](#)]
23. Stanford, N.; Bate, P. Crystallographic variant selection in Ti-6Al-4V. *Acta Mater.* **2004**, *52*, 5215–5224. [[CrossRef](#)]
24. Van Bohemen, S.; Kamp, A.; Petrov, R.; Kestens, L.; Sietsma, J. Nucleation and variant selection of secondary  $\alpha$  plates in a  $\beta$  Ti alloy. *Acta Mater.* **2008**, *56*, 5907–5914. [[CrossRef](#)]
25. Bhattacharyya, D.; Viswanathan, G.; Denkenberger, R.; Furrer, D.; Fraser, H.L. The role of crystallographic and geometrical relationships between  $\alpha$  and  $\beta$  phases in an  $\alpha/\beta$  titanium alloy. *Acta Mater.* **2003**, *51*, 4679–4691. [[CrossRef](#)]
26. Takajo, S.; Brown, D.W.; Clausen, B.; Gray, G.; Knapp, C.M.; Martinez, D.T.; Trujillo, C.P.; Vogel, S.C. Spatially resolved texture and microstructure evolution of additively manufactured and gas gun deformed 304L stainless steel investigated by neutron diffraction and electron backscatter diffraction. *Powder Diffr.* **2018**, *33*, 141–146. [[CrossRef](#)]
27. Tiferet, E.; Ganor, M.; Zolotaryov, D.; Garkun, A.; Hadjadj, A.; Chonin, M.; Ganor, Y.; Noiman, D.; Halevy, I.; Tevet, O.; et al. Mapping the tray of electron beam melting of Ti-6Al-4V: Properties and microstructure. *Materials* **2019**, *12*, 1470. [[CrossRef](#)] [[PubMed](#)]
28. Wenk, H.R.; Lutterotti, L.; Vogel, S. Texture analysis with the new HIPPO TOF diffractometer. *Nucl. Instrum. Methods Phys. Res.* **2003**, *515*, 575–588. [[CrossRef](#)]
29. Vogel, S.C.; Hartig, C.; Lutterotti, L.; Von Dreele, R.B.; Wenk, H.R.; Williams, D.J. Texture measurements using the new neutron diffractometer HIPPO and their analysis using the Rietveld method. *Powder Diffr.* **2004**, *19*, 65–68. [[CrossRef](#)]
30. Rietveld, H.M. A profile refinement method for nuclear and magnetic structures. *J. Appl. Crystallogr.* **1969**, *2*, 65–71. [[CrossRef](#)]
31. Lutterotti, L.; Matthies, S.; Wenk, H.R.; Schultz, A.; Richardson, J., Jr. Combined texture and structure analysis of deformed limestone from time-of-flight neutron diffraction spectra. *J. Appl. Phys.* **1997**, *81*, 594–600. [[CrossRef](#)]
32. Wenk, H.R.; Lutterotti, L.; Vogel, S. Rietveld texture analysis from TOF neutron diffraction data. *Powder Diffr.* **2010**, *25*, 283–296. [[CrossRef](#)]
33. Nowell, M.M.; Field, D.P.; Wright, S.I.; Dingley, D.; Scutts, P.; Suzuki, S. Orientation Imaging of Recrystallization, Grain Growth and Phase Transformations using In-Situ Heating. *Microsc. Microanal.* **2005**, *11*, 1494–1495. [[CrossRef](#)]

34. Takajo, S.; Merriman, C.; Vogel, S.; Field, D. In-situ EBSD study on the cube texture evolution in 3 wt.% Si steel complemented by ex-situ EBSD experiment—From nucleation to grain growth. *Acta Mater.* **2019**, *166*, 100–112. [[CrossRef](#)]
35. Tomida, T.; Vogel, S.C.; Onuki, Y.; Sato, S. Texture Memory in Hexagonal Metals and Its Mechanism. *Metals* **2021**, *11*, 1653. [[CrossRef](#)]
36. Burgers, W. On the process of transition of the cubic-body-centered modification into the hexagonal-close-packed modification of zirconium. *Physica* **1934**, *1*, 561–586. [[CrossRef](#)]
37. Bunge, H.; Humbert, M.; Welch, P. Texture transformation. *Textures Microstruct.* **1984**, *6*, 81–95. [[CrossRef](#)]
38. Bunge, H.J.; Esling, C. Quantitative texture analysis. In *Deutsche Gesellschaft für Metallkunde, v+ 551, 24 x 17 cm, illustrated(DM 168.00)*; DGM Informationsgesellschaft: Oberursel, Germany, 1982.
39. Inoue, H. Standardization of Measurement and Representation in Texture Analysis. *Mater. Jpn.* **2001**, *40*, 589–591. (In Japanese) [[CrossRef](#)]
40. Tomida, T.; Wakita, M.; Yasuyama, M.; Sugaya, S.; Tomota, Y.; Vogel, S. Memory effects of transformation textures in steel and its prediction by the double Kurdjumov–Sachs relation. *Acta Mater.* **2013**, *61*, 2828–2839. [[CrossRef](#)]
41. Zeng, L.; You, C.; Wang, C.; Zhang, X.; Liang, T. Simultaneously enhancing the strength and ductility of lamellar Ti–6Al–4V alloy via designing hierarchical 3D nanolayered structure. *Mater. Lett.* **2020**, *261*, 127020. [[CrossRef](#)]
42. Safdar, A.; Wei, L.Y.; Snis, A.; Lai, Z. Evaluation of microstructural development in electron beam melted Ti-6Al-4V. *Mater. Charact.* **2012**, *65*, 8–15. [[CrossRef](#)]
43. Gil, F.; Ginebra, M.; Manero, J.; Planell, J. Formation of  $\alpha$ -Widmanstätten structure: Effects of grain size and cooling rate on the Widmanstätten morphologies and on the mechanical properties in Ti6Al4V alloy. *J. Alloys Compd.* **2001**, *329*, 142–152. [[CrossRef](#)]
44. Zhang, S.; Li, J.; Kou, H.; Yang, J.; Yang, G.; Wang, J. Effects of thermal history on the microstructure evolution of Ti-6Al-4V during solidification. *J. Mater. Process. Technol.* **2016**, *227*, 281–287. [[CrossRef](#)]
45. Senkov, O.; Valencia, J.; Senkova, S.; Cavusoglu, M.; Froes, F. Effect of cooling rate on microstructure of Ti-6Al-4V forging. *Mater. Sci. Technol.* **2002**, *18*, 1471–1478. [[CrossRef](#)]
46. Filip, R.; Kubiak, K.; Ziąja, W.; Sieniawski, J. The effect of microstructure on the mechanical properties of two-phase titanium alloys. *J. Mater. Process. Technol.* **2003**, *133*, 84–89. [[CrossRef](#)]
47. Neikter, M.; Åkerfeldt, P.; Pederson, R.; Antti, M.L.; Sandell, V. Microstructural characterization and comparison of Ti-6Al-4V manufactured with different additive manufacturing processes. *Mater. Charact.* **2018**, *143*, 68–75. [[CrossRef](#)]
48. Zeng, L.; Bieler, T. Effects of working, heat treatment, and aging on microstructural evolution and crystallographic texture of  $\alpha$ ,  $\alpha'$ ,  $\alpha''$  and  $\beta$  phases in Ti–6Al–4V wire. *Mater. Sci. Eng. A* **2005**, *392*, 403–414. [[CrossRef](#)]
49. Wang, X.; Chou, K. EBSD study of beam speed effects on Ti-6Al-4V alloy by powder bed electron beam additive manufacturing. *J. Alloys Compd.* **2018**, *748*, 236–244. [[CrossRef](#)]